In-flight calibration and monitoring of the TROPOMI-SWIR module

Tim A. van Kempen[1], **Richard M. van Hees**[1], **Paul J.J. Tol**[1], **Ilse Aben**[1,2], **and Ruud W.M. Hoogeveen**[1]

[1]SRON Netherlands Institute for Space Research, Sorbonnelaan 2, 3584 CA, Utrecht, the Netherlands
[2]Vrije Universiteit, Faculty of Science, De Boelelaan 1085, 1081 HV, Amsterdam, the Netherlands

Correspondence: Tim van Kempen (t.a.van.kempen@sron.nl)

Abstract. During its first year in operation the short-wave infrared (SWIR) tropospheric monitoring instrument (TROPOMI) was calibrated in-flight and its performance was monitored. In this paper we present the results of the in-flight calibration and the ongoing instrument monitoring. This includes the determination of the background signals, noise performance, instrument spectral response function (ISRF) stability and stray-light stability. From these results, the number of incurred dead and bad pixels due to cosmic-ray impacts is determined. The light-path transmission is checked by monitoring internal lamp and diffuser stabilities. Due to its high sensitivity for Earth radiation on the eclipse side, the calibration strategy for the background (i.e. dark current and offset) monitoring was adjusted. Trends over the first full year of nominal operations reveal a very stable SWIR module. The number of newly incurred dead and bad pixels is less than 0.1% over nearly a full year since the start of operations. Assuming linear degradation of various components, the SWIR module is expected to keep performing within expected parameters for the full operational lifetime.

---

1 Introduction

The Sentinel-5 Precursor mission (Veefkind et al., 2012, better known as S5P), is the first mission within the scope of the European Union Copernicus program[1] dedicated to mapping and monitoring of the chemical composition of the Earth's atmosphere. S5P is a precursor mission for the atmospheric composition Sentinel-5 missions, which produces the same global coverage as S5P. The Sentinel-5 mission are scheduled to launch in 2022 and beyond. The Tropospheric Monitoring Instrument (TROPOMI[2]) is the sole instrument onboard S5P. It consists of two modules: a ultra-violet, visible and near-infrared (UVN) module (Veefkind et al., 2012) and a SWIR module[3] (Hoogeveen et al., 2013). The wavelength ranges include the spectral signatures of key trace gases that strongly influence climate and air quality. The SWIR module is aimed at measuring column densities of carbonmonoxide (CO) and methane (CH_4). Hoogeveen et al. (2013) presented the detector performance. TROPOMI produces daily global coverage column density maps of these gases using a swath of approximately 2600 km across track. Images are taken each 1.08 seconds yielding spatial pixels of approximately 7 by 7 km^2 at nadir. Note that since August 16th 2018 the resolution of TROPOMI could be improved; Images are taken at 0.8 seconds yielding spatial pixels of approximately 7 by 5.5 km^2 at nadir. The SWIR spectral range (2305-2385 nm) is sampled at 0.1 nm, while the spectral resolution is 0.22 nm.

With a total envisioned lifetime of 7 years, the mission will provide a unique insight into the chemical composition of our atmosphere. TROPOMI will be an essential tool to investigate both natural and anthropogenic induced chemical

---

[1]see http://www.copernicus.eu

[2]TROPOMI is a collaboration between Airbus Defence and Space Netherlands, KNMI, SRON and TNO, on behalf of NSO and ESA. Airbus Defence and Space Netherlands is the main contractor for the design, building and testing of the instrument. KNMI and SRON are the principal investigator institutes for the instrument. TROPOMI is funded by the following ministries of the Dutch government: the Ministry of Economic Affairs, the Ministry of Education, Culture and Science, and the Ministry of Infrastructure and the Environment.

[3]The SWIR spectrometer was developed by SSTL under an Airbus-Dutch Space contract, with contributions of SRON and Sofradir.

variations at timescales from days to years.

S5P was launched on October 13th 2017, from Plesetsk, Russia, into an ascending sun-synchronous orbit with an equator crossing time at 13:30 Mean Local Solar time at an altitude of approximately 824 km. After launch, the first month was dedicated to outgassing and stabilization. TROPOMI was kept warm to prevent the detector (in particular the SWIR detector) to act as a cold trap and thus avoid contamination; the S5P cooler door was opened on November 7th 2017. In the following week, the SWIR detector and spectrometer cooled down to their operational temperatures of 140 K and 202 K respectively.

Between the launch and April 30th 2018, the commissioning phase, also referred to as phase E1, was carried out with the aim to complete the calibration of the instrument, check the data processing chain and prepare for the nominal operations phase, referred to as phase E2. Nominal operations started at orbit number 2818. During nominal operations, it is necessary to monitor the instrument calibration derived on-ground. This is done using measurements in the eclipse side of each orbit. TROPOMI covers the entire planet Earth each day in 14.5 orbits. For the SWIR module, monitoring is performed for the background signal, the instrumental noise, the quantification of the pixel quality, validation/monitoring of the instrumental spectral response function (ISRF) and stray-light correction. Correction are based on so-called Calibration Key Data (CKD). The ISRF correction algorithm, the on-ground calibration and the ISRF CKD (Calibration Key Data) derivation are reported in van Hees et al. (2018). All elements of the the stray-light correction, including the CKD derivation, can be found in Tol et al. (2018). CKDs for offset, dark-current, noise and pixel quality were derived on-ground. Signals of the sun as seen over the two diffusers and signals of the internal lamps are monitored to quantify any transmission changes of various components within the SWIR module.

In this paper we will report on the results of the commissioning phase, the monitoring during the first full year of nominal operations and provide an outlook of the durability and future performance of the SWIR module. The outline of the paper is as follows. Section 2 details the calibration plan. Section 3 presents the results of the commissioning phase. Section 4 describes the monitoring results and trends of the first year of TROPOMI. Finally, the conclusions are given in section 5.

2   In-flight Calibration and Monitoring Plan

2.1   Calibration Plan

The calibration of SWIR is done primarily using data obtained during the on-ground calibration campaign (Kleipool

et al., 2018). It is a key part of the calibration plan to monitor the quality of the results obtained from these on-ground calibrations over the lifetime of TROPOMI and update procedures and/or the CKDs if necessary.

There are several types of measurements available for in-flight calibration:

- spectral radiance (i.e. backscattered and/or thermal radiation from the Earth, available for both for the day and night-side). This includes background measurements taken in the eclipse with an open folding mirror (FMM).

- measurements with a closed FMM, looking into the on-board calibration unit (CU).

- spectral irradiance (i.e. radiation from the sun)

The spectral irradiance signal passes over one of two diffusers to scale the signal to measurable levels. The first diffuser is used daily to measure the signal. The second diffuser is used weekly, thus enabling the detection and/or monitoring of degradation of the first diffuser.

With the FMM is closed, the SWIR module can be illuminated by several on-board calibration sources installed specifically for in-flight monitoring of calibration parameters. This is done by rotating the central diffuser carousel. In addition to the background measurements (i.e. all sources turned off), the following on-board illumination sources are relevant[4] for the SWIR module:

- DLED - a dedicated detector LED emitting with a known smooth spectral profile at the SWIR wavelengths.

- WLS - White Light Source

- SLS - Spectral Line Source: five dedicated diode lasers in the SWIR spectral band

The DLED (deterctor LED) is placed in front of the detector behind the immersed grating, while the SLS and WLS are located in the calibration unit and thus follow almost the complete optical path. This is an important difference to distinguish effects of the full optical path, or of the detector only.

The five on-board tune-able distributed feedback lasers, or SLS, are unique to the SWIR module. These lasers are able to scan small parts of the wavelength range by changing the laser temperature using a thermo-electric cooler integrated into the laser housing. The range is about 70 detector pixels ($\sim$7 nm), Due to operational constraints, the laser scan is done over 0.6 nm with a fixed diffuser (see van Hees et al. (2018) for more details on the capability of the SLS diffuser to be used in either fixed or oscillating mode.). The central

---

[4]Note that a CLED is within the light path of the SWIR detector (Kleipool et al., 2018). However, the emission properties of the CLED shows it does not emit any light at SWIR wavelengths and is thus not relevant for SWIR calibration.

wavelength of each laser has been selected to be able to sample different parts of the SWIR wavelength range. The signal of the SLS passes over a dedicated diffuser. This diffuser can be employed in oscillation mode to suppress speckles observed in the laser signal or in fixed mode. Due to a limited operational lifetime and excess heat produced by the oscillating diffuser, the calibration plan is to not oscillate the diffuser during nominal operations (van Hees et al., 2018). The location and light paths into the SWIR module of the on-board illumination sources are shown in Figure 1. The DLED is located inside the SWIR module.
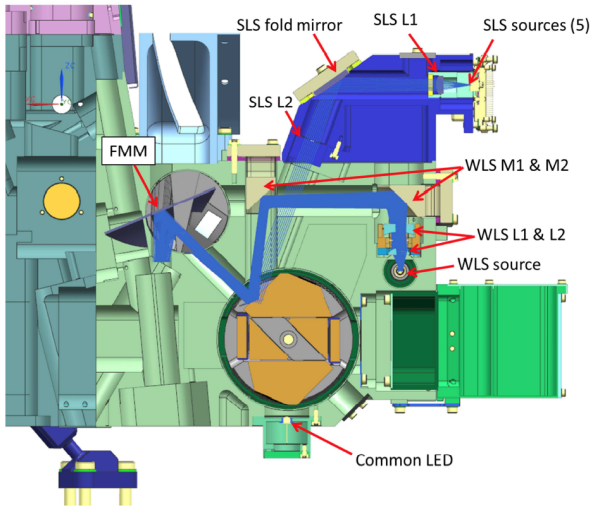
Figure 1. Instrument layout indicating the location of the on-board illumination sources. The light paths of the SLS and WLS are shown in blue lines. The DLED is located within the SWIR module. The location of the CLED is shown. However, as it is not emitting any light at SWIR wavelengths, it is not used for SWIR calibration or monitoring. Figure courtesy of Airbus Defense and Space Netherlands and TNO.

Table 1 lists the parameters for which calibration parameters, the CKD, or monitoring data are derived. Measurements are taken in-flight to monitor whether the CKD can still be applied correctly during data processing. For calibration, we identify static, dynamic and monitoring quantities. Static CKDs are not dynamically updated in the processor following measurement results, while dynamic CKDs are automatically updated. Static can be manually adjusted if warranted. Monitoring quantities are only monitored, but do not have a direct relation to CKD parameters. However, changes in these parameters will often initiate analysis in the applicability of the current calibration. Monitoring of all these quantities is essential for the health monitoring of the SWIR module. Currently all CKDs are static.

2.2 Processing Chain

Science signals of TROPOMI SWIR are taken from a detector array consisting of 1000 pixels in the spectral dimension

| Quantity	CKD Type	Measurements
Dark current	Static	Dark
Offset	Static	Dark
Noise	Static[1]	Dark
Quality[2]	Static	-
Lamp Stability	Monitor	DLED/WLS/SLS
PRNU[3]	Static	DLED/WLS
Diffuser Stability	Monitor	Irradiance
Transmission	Monitor	DLED/WLS/Irrad.
ISRF	Monitor [4]	SLS
Stray-light	Static	SLS

Table 1. Calibration and monitoring data obtained in-flight

[1] The Noise CKD is static. However, the in-flight noise of the detector is measured dynamically as input for the monitoring of the quality. Readnoise was derived on-ground.
[2] The quality map does not use direct measurements, but uses the dynamically measured dark current and in-flight noise.
[3] The PRNU (pixel to pixel non-uniformity) stability is included in the comparison of the different light sources.
[4] The ISRF is not used in the L1b data processing, but used in the SWIR retrievals such as CO or CH_4.
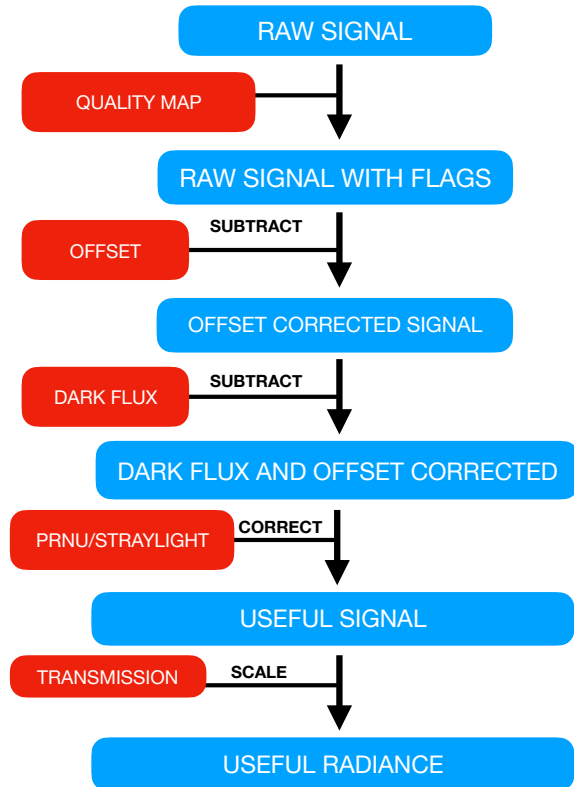
Figure 2. Summary flow chart of the processing chain of a SWIR signal. This describes the processes that require monitoring in-flight. It assumes unit conversions are correctly carried out to produce useful radiance in spectral radiance units.

(columns) and 250 pixels in the spatial dimension (rows) of which 960 columns and 215 rows can be illuminated. Each pixel is read out individually through a CMOS read-out IC (Hoogeveen et al., 2007), but the exposure time is identical for all pixels in the detector. Exposure times during nominal operations range from 82 ms to typically 1080 ms. Shorter exposure times are used to avoid detector saturation in case of high input light levels. For reference to be used in the remainder of the paper: a pixel signal can be between 0 and 500,000 electrons, leading to electrical signals between 0.5 and 3.5 Volts, digitized typically with 12,000 Binary Units (BU). A raw TROPOMI-SWIR signal consists of three components: an offset, which is independent of exposure time; a dark signal, which is dependent on exposure time; and an outside signal. Outside signal can either be the Earth radiance, Solar irradiance or signal from the on-board lights. Outside signal includes straylight. To accurately derive the useful signal (i.e., the outside signal) the offset and dark current signals must be determined to high precision and in turn subtracted from the raw signal. To calibrate the useful signal, the outside signal has to be corrected for with several factors that influence the signal, such as the transmission (i.e. due to degrading of components in the optical path, possibly resulting in light lost), pixel response non-uniformity (PRNU) and influence of stray-light. Stray-light is defined as any outside signal that does not follow the intended path onto the detector and is thus not part of the useful signal. It may include ghosts, out of field stray-light, out of (spectral) band stray-light or other forms. Stray-light correction for the SWIR module is extensively discussed in Tol et al. (2018). In-flight stray-light monitoring is discussed in section 3.5.

Hoogeveen et al. (2013) mentions a few other effects as observed in the SWIR detector. A small pixel-memory correction is applied when the exposure time is equal to the cycle time (i.e. 1080 or 800 ms). With faster detector readout, data are typically co-added, making the memory error smaller, and more difficult to correct for. Therefore, co-added data are not corrected for memory effects. Given the range of typical exposure times, non linearity of the detector was judged to be too small to justify a complex correction algorithm. The wavelength calibration is not specifically monitored, but follows from trace gas retrieval algorithms where small wavelength shifts are fitted within the procedure. The flow chart in Figure 2 summarizes the full SWIR calibration processing.

3   In-flight Calibration during the commissioning phase

3.1   Dark current and Offset

3.1.1   Method

The value of the offset en dark-current corrections are determined from measurements at the eclipse side of the orbit, see Table 1. Measurements are carried out with identical instrument settings (exposure time and co-adding factor) as the radiance measurements on the solar illuminated side of the orbit. The exposure times range from 178 ms over the equator to 538 ms over the poles. Before launch, it was assumed the eclipse side of the Earth is dark and the raw signal is composed only of the offset and dark current[5]. A linear fit using measurements at a range of exposure times will yield the offset (signal at exposure time zero) and dark current (slope of the fit). In total, derivations are done every 15 orbits, using all background measurements within those 15 orbits.

3.1.2   Background with FMM open

Figure 3 and 4 shows the radiance of the SWIR continuum at 2314 nm at the eclipse side of the orbit around two regions: the northern part of the Persian Gulf and north-western Australia. Data were taken from orbits 430 and 433, measured during the first-light campaign during November 2017. All exposure times were 216 ms.

In both scenes of Figure 3 and 4 small regions and point sources are clearly visible with signals more than an order higher than the background. Given the location, the sources are most likely the burning of excess natural gas at oil field installations (Basra) or natural wildfires (Australian outback). Inspection of other data yields many other emission sources over land including other bush fires and volcanic activity.

At larger spatial scales, thermal radiation of the Earth at night is detected by the SWIR module both over land and over oceans. Thermal radiation of the oceans appears brighter, presumably due to inherently longer cooling times of water. However, even at high latitudes, radiances are clearly nonzero at the eclipse side of the orbit.

Figure 5 presents the dark current at detector level using measurements with the FMM open. The top plot shows the results, while the bottom row shows the difference with the dark current derived from the on-ground calibration. Statistics of the results over the entire detector, i.e. the biweight median and spread[6], are given in Table 2. The comparison reveals the following:

– The overall structure of the dark current on the detector is reproduced, see Hoogeveen et al. (2013).

– The median over the detector is somewhat lower (61 e/s).

– The difference in spreads is significant due to the amount of data used in obtaining the results.

---

[5]Note in this paper, we define the dark current as the combination of the true dark current (i.e. the current produced by the detector at its operational temperature) and the signal from the thermal background of the surrounding instrument components.

[6]Throughout this paper, the biweight median and biweight spread are used. For simplicity the terms median and spread are used throughout. Biweight median is a statistical parameter described in Beers et al. (1990).
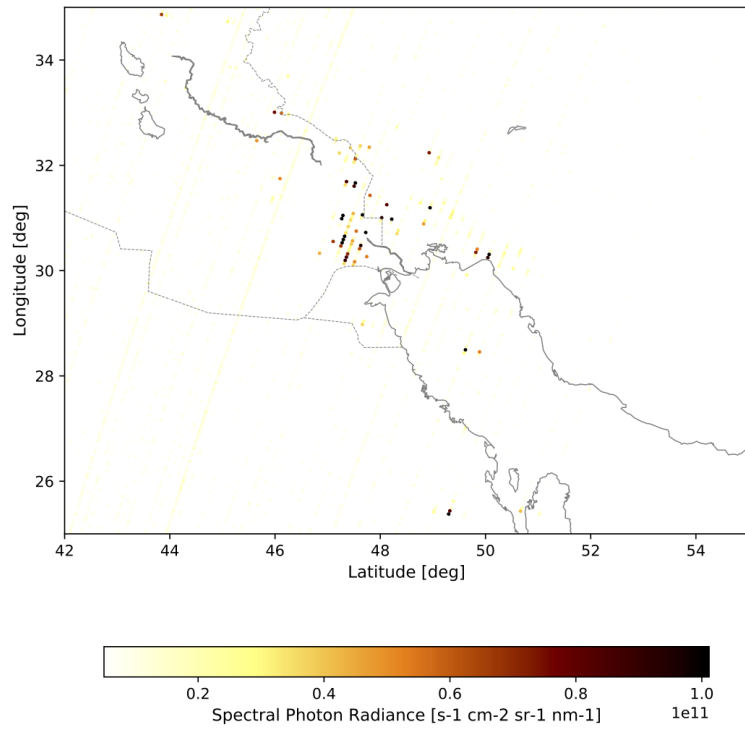
Figure 3. Continuum radiance at 2314 nm at the eclipse side of the Earth around the Iraqi city of Basra Any stripes are limitations of calibration and thermal stability at the time. Localized enhanced signals are clear indications of emission sources on Earth.
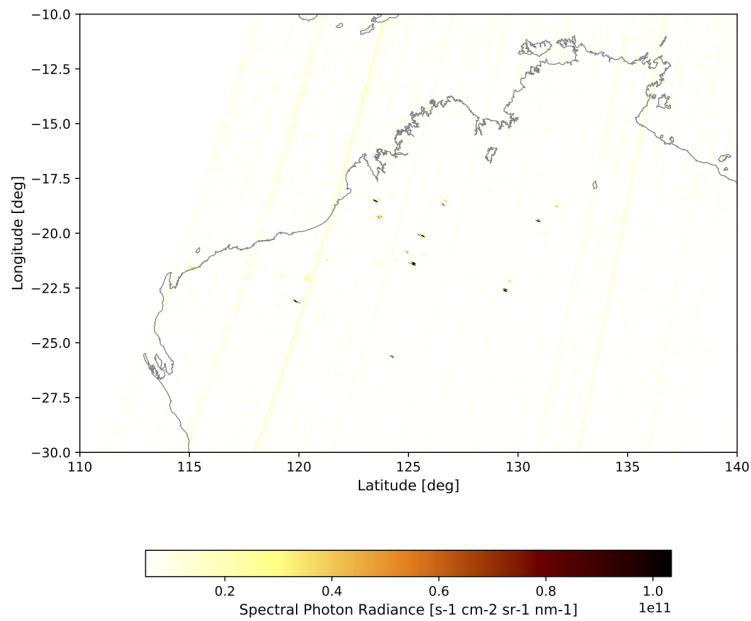
Figure 4. Continuum radiance at 2314 nm at the eclipse side of the Earth for the north-western Australian outback. Any stripes are limitations of calibration and thermal stability at the time. Localized enhanced signals are clear indications of emission sources on the Earth.
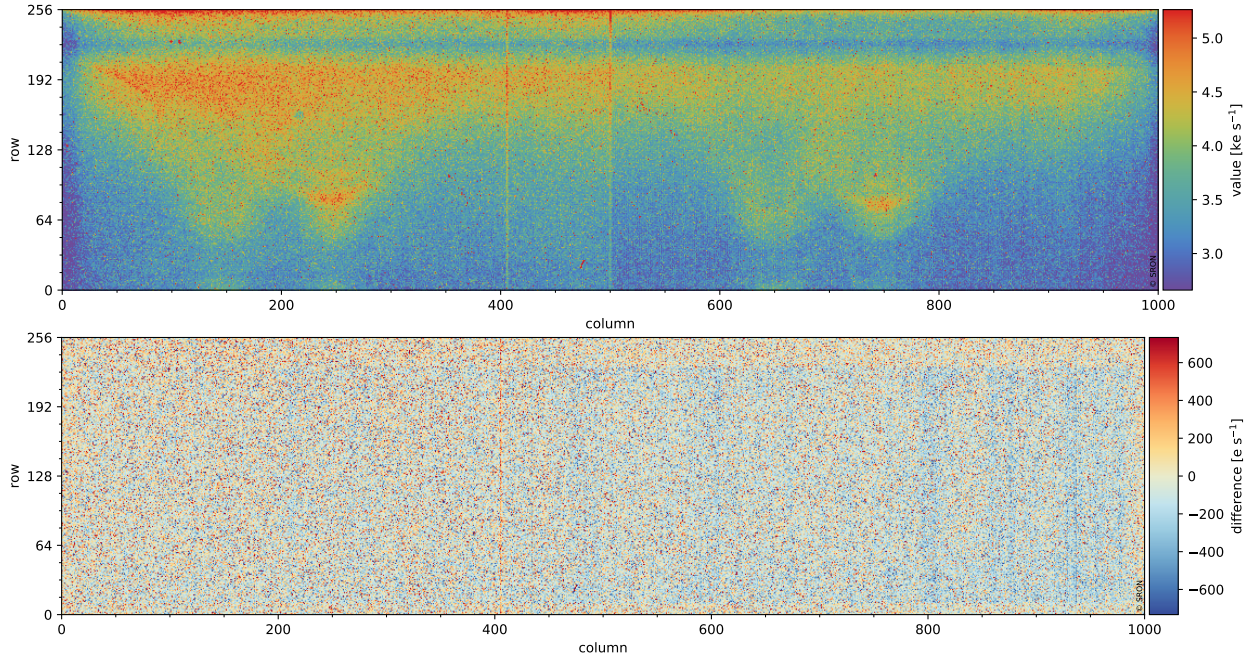
Figure 5. Typical dark current obtained with FMM open during the commissioning phase using data from orbits 990 to 1004 can be seen in the top plot. Data are plotted over the detector with the horizontal axis equivalent to the spectral direction and the vertical axis the spatial swath. The bottom plot shows the result with the on-ground results subtracted.

– Specific spectral features can be seen in the comparison to the on-ground calibration Fig. 5 in the form of blue bands. The wavelengths correspond to deep absorption bands of water and methane in the atmosphere. No atmosphere was present during the on-ground reference measurements. The detector temperatures in-flight and on-ground were identical. Thus, absorption of the Earth's thermal radiation by water and methane occurs, causing this difference. These also do not extend to the top and bottom rows, which are covered.

– stronger differences are seen in columns 400 and 500. Column 500 is due to the edge of the ADC areas. The difference in column 400 is unexplained.

Analysis of a range of measurements over 3 months also revealed differences with the on-ground calibration results to vary in time by ∼20 e/s. No trend was seen, but local changes in e.g. Earth's temperature field or weather can influence the results. These are partially mitigated by taking a bi-weight median over all available data, but this method cannot completely remove these effects.

The amount of dark current detected differs from the measured value reported in Hoogeveen et al. (2013). They present a median in the central area of 0.7 fA, equivalent to 4400 electrons per second. This is likely attributed to the different thermal conditions of the setup, as a significant part of the dark current is caused by the thermal emission of the spectrometer, which was absent in Hoogeveen et al. (2013).

The non-uniformity of the Earth's thermal radiation also introduces another significant bias. As most calibration measurements are taken near the warmer equator, the measurements are not representative for the complete orbit including the polar regions.

Origin	Orbit	Median [e/s]	Spread [e/s]	On-ground Diff. [e/s]
FMM open	1004	3736	14.4	61
FMM closed	2721	3772	20.3	-25
Nominal operations	7778	3764	16.5	-33

Table 2. Median and spread of the various dark currents (nominal operations are with FMM closed) and comparison with the median of on-ground calibration. Difference is defined as on-ground minus the measurement. The on-ground results are based on many more measurements. As such the uncertainties calculated from the spread are not comparable.
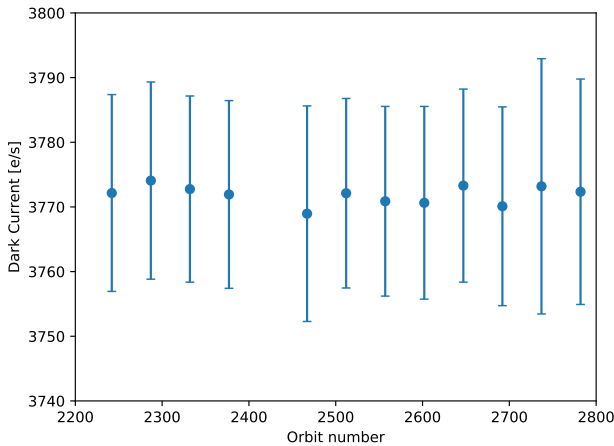
3.1.3 Dark current with FMM closed

Given the issues described in section 3.1.2, background measurements were also performed with the FMM closed.

Figure 6 shows the derived dark current with the FMM closed, and its comparison with the on-ground result. The detector median is given in Table 2. With the FMM closed, dark current does not differ significantly with the on-ground results.
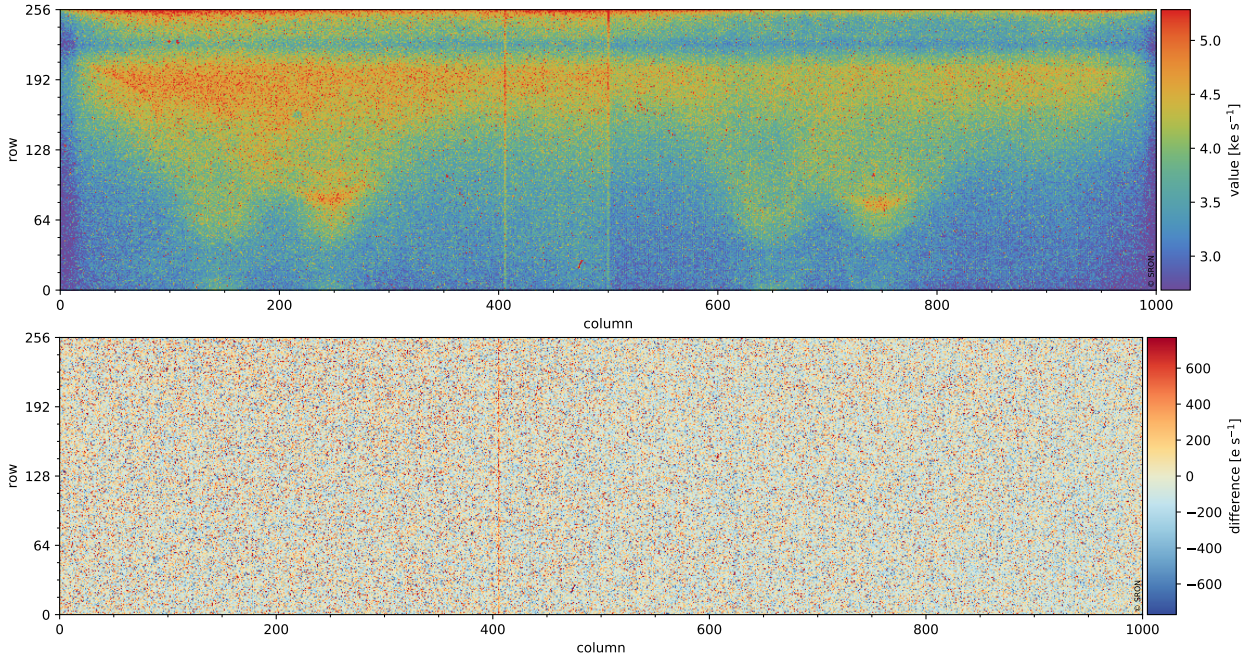
Figure 6. Typical dark current obtained with FMM closed at the start of the nominal operations phase using data from orbits 2818 to 2833 can be seen in the top plot. Data are plotted over the detector with the horizontal axis equivalent to the spectral direction and the vertical axis the spatial swath. A comparisons to the dark current derived during the on-ground calibration is shown in the bottom plot.

Figure 7. Median dark current and its uncertainty obtained with FMM closed at the start of the nominal operations phase between orbits 2200 to 2800 (end of the commissioning phase) as a function of time. The shown length of time is about six weeks. Note that due to the structure seen in the dark current, the spread (not shown) is much larger.

Averaged over the entire detector, the dark current is lower by ∼25 e/s than the on-ground measurements. This is likely due to different thermal conditions. Another difference with the on-ground results is found in the spread (i.e. the uncertainty of the fit). This is caused due to the number of input points for each fit. Both the number of different exposure times as well as the amount of the measurements available for each exposure time was higher during the on-ground calibration. However, the detected systematic differences between on-ground and in-flight with the FMM open, such as the absorption bands or latitude dependent signal are clearly absent when the FMM is closed.

The dark current with the FMM closed was also tracked in time over the last two months of the commissioning phase. Derivations were carried out at intervals of 15 orbits with the requirement that at least 40% of all orbits contained background measurements. Figure 7 reveals that the dark current with the FMM closed is very stable with variations of 2-3 electrons per second from derivation to derivation. The uncertainty can vary depending on the total amount and total length of the measurements included each interval.

3.1.4 Orbital Dark

During nominal operations, measurements are typically taken at northern latitudes of the eclipse side of the orbit. As such, any variation within a single orbit cannot be monitored or calibrated. This may lead to a systematic error if there are thermal variations within a single orbit. Accurate calibration of the dark current thus includes a calibration of thermal variations as a function of the orbital phase[7], using background measurements over a several orbits with the FMM closed.

---

[7]Orbital phase is a number between 0 and 1 defining at which point after orbital midnight the spacecraft is located within a single orbit.

The observed signal with the FMM closed as a function of orbital phase was inspected at exposure times of 100, 500 and 1000 milliseconds. The data show no dependency of the dark current over the orbit. Therefore, no orbital variation of the dark-current correction is applied in the data processor. Two increases in the signal were detected, both during overpasses of the South Atlantic Anomaly (SAA) region. Within the SAA, the van Allen radiation belt dips much closer to the surface of the planet, significantly increasing the amount of cosmic radiation hits on the detector and thus leading to a small increase in average background signal. All measurements in the SAA are flagged as less reliable.

3.1.5   Conclusions on FMM setting

In conclusion, background measurements with the FMM closed produce more accurate and more stable dark currents than measurements with the FMM open. Surface features, such as fires and the land–sea difference, are removed from background measurements if the FMM is closed. In addition, the accidental introduction of spectral features due to methane and water absorption in the thermal radiation is also removed. When the data taken in the SAA are excluded from the analysis, no orbital dependency of the dark signal is necessary. Nominal operations was adapted to include this recommendation. Dark current is also shown to have similar values as measured during the on-ground calibration as well as the values reported in the detector characterization (Hoogeveen et al., 2013).

3.1.6   Offset

Since the offset is derived using the same set of measurements as the dark current, the offset of the SWIR detector shows similar dependencies as the dark current. All conclusions for the dark current also apply to the offset. Figure 8 and 9 show the offset with the FMM closed and its dependency on time as a reference. Note that there appears a small systematic difference between the two analogue digital converters (ADC), each covering a half of the detector, which is not well understood, but currently attributed to different thermal conditions. This difference is within the limits of the defined requirements.

3.2   In-flight Noise

The noise on all signals read is composed of three components: (i) shot noises of the external signal, thermal background and dark current, (ii) Johnson noise and (iii) readnoise. These combine to form the total noise. Readnoise is independent of exposure time, while the other noise components depend on the exposure time. Readnoise was calibrated during the on-ground calibration campaign by measuring the noise versus exposure time and extrapolating back to zero exposure time. The other noise components are grouped as in-flight noise. It is necessary to measure the in-flight noise of each pixel without any external signal or its shot noise as input for the detector pixel quality monitoring. Detector pixels with too high noise levels (either readnoise or in-flight noise) are not be used for retrieval of CO or CH_4.

Early in the E1 phase, in-flight noise calibration measurements were executed with the FMM open, similar to the dark current and offset. However, similar effects were seen for the noise as discussed in section 3.1, with signals from point sources and non-uniform Earthshine influencing the noise derivations. Therefor, calibration measurements to determine noise levels are also be executed with the FMM closed during nominal operations.

Figure 10 shows the in-flight noise with the FMM closed, taken 6 months after launch. Noise can be derived either by taking the standard deviation over all frames within a measurement, with the median subtracted, or the spread of all frames. For a symmetric gaussian distribution of the data points, both methods yield an identical result. But for a skewed distribution with outliers, the standard deviation method tends to result in a higher noise than the bi-weight median. In Figure 10, both are plotted. For the SWIR module, most outliers are produced by cosmic ray impacts that manifest themselves as dots and small tracks in Figure 10.

Figure 11 shows the comparison between the readnoise CKD as measured on-ground and the one measured in-flight. Figures are shown using derivations with a standard deviation and a bi-weight spread, highlighting the impact of cosmic rays.

### 3.3   Detector Pixel Quality

The quality map of the SWIR detector details how many detector pixels are of sufficient quality to be included in retrieval algorithms. In the definition of ′sufficient quality′, a pixel should

– have a inear response to light as a function of exposure time.

– not show excessive noise.

– not produce excessive dark current

Excessive was defined as more than three times the spread higher than the median over the array. However, this definition will be reviewed in-flight. Using a weighted function (for which the weighting was determined using on-ground calibration measurements), each pixel is graded with a number between 0 (completely dead or unusable pixel) and 1 (perfectly working) using measurements of the noise and dark current. A detector pixel is considered to be bad if this value is lower than 0.8. A ′dead′ category is tracked by considering detector pixel with values below 0.1[8]. If required, manual

---

[8]Note that the dead category includes, but is not limited to, pixels with no response (i.e. a value of 0.0). ′Dead′ pixels with a nonzero quality grading can improve to a higher grading such as ′bad′
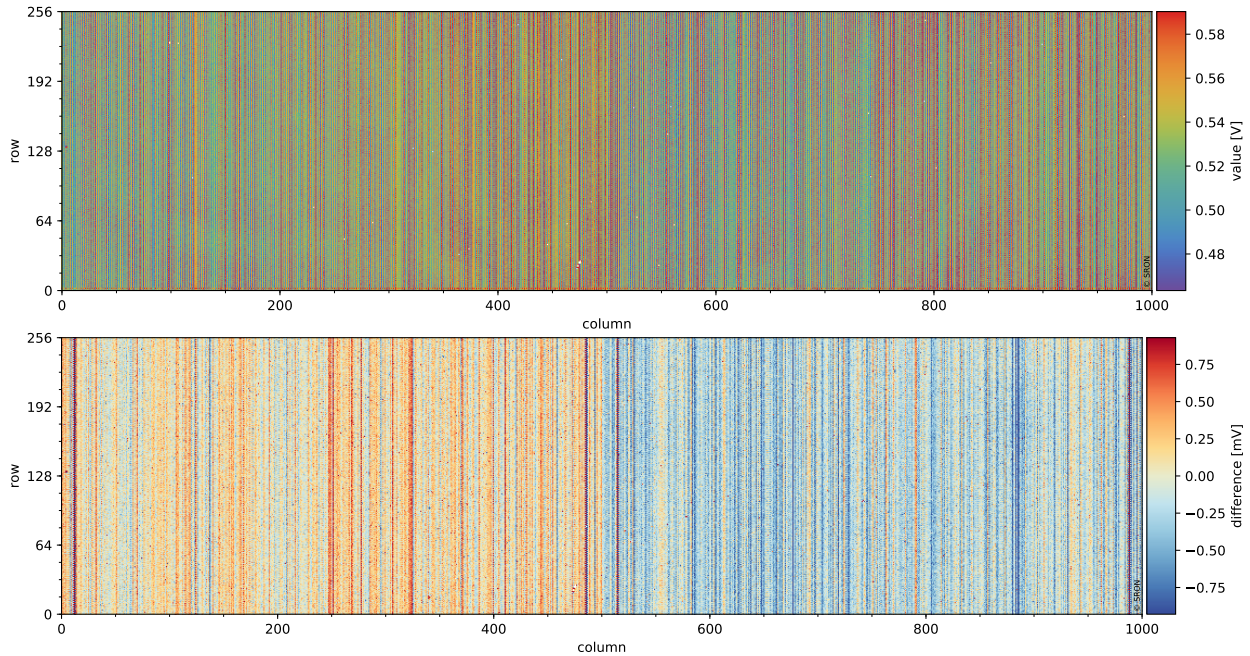
Figure 8. Offset obtained with FMM closed during the E1 phase using data from orbits 2707 to 2721 can be seen in the top plot. Data are plotted over the detector with the horizontal axis equivalent to the spectral direction and the vertical axis the spatial swath. A comparison to the offset derived during the on-ground calibration is shown at the bottom plot.
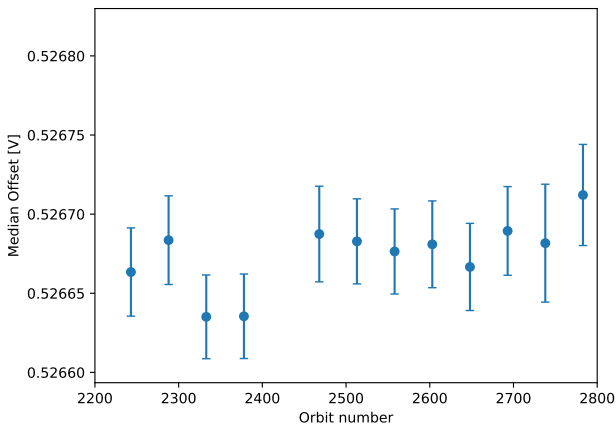
Figure 9. Median offset and its uncertainty obtained with FMM closed during the E1 phase between orbits 2200 to 2800 as a function of time.

flagging is also possible within the processor (i.e. setting this quality to 0.0). Some pixels were known to be not functional even before launch. For simplicity, the definition of not functional includes pixels outside of the effective area which are not illuminated, but are technically functional. These were manually set to 0.0.Note that pixels are excluded from any trend plots such as shown in Fig. 12. It is expected that other

and are thus not truly dead. However, for simplicity, we have limited ourselves to these three categories.

pixels may become unusable over time (e.g., no signal, too noisy) due to cosmic ray impacts or hardware degradation.

Figure 12 shows the number of flagged pixels at the end of the commissioning period. Only data from orbit 1800 and later were analysed as data were taken in a consistent procedure with the FMM closed. An open FMM, heavily influenced the dark and noise, and thus the quality. This quality map is derived using a bi-weight median noise, given the limitations discussed above. Table 3 lists the number of pixels identified both on-ground, during the the commissioning phase and at the start of nominal operations. Note that the quality is derived using all available data once per 15 orbits. Interestingly, the number of 'bad' and 'dead' pixels decreased after launch. This likely has several causes. First, the thermal environment during the on-ground calibration and the in-flight measurements (taken 1800 orbits after launch, which equals over 4 months) is known to have been different. Second, the instrument settings of many of the on-ground calibration measurements have been (subtly) different then used in-flight. Third, the detector underwent an annealing as it was launched warm. Last but not least, the algorithm used to derive offset and dark current was improved between the on-ground calibration and the end of E1.

3.4 Transmission

The stability of the transmission of the optical components is checked by comparing the signal of various on-board calibration sources and the solar irradiance measured with the
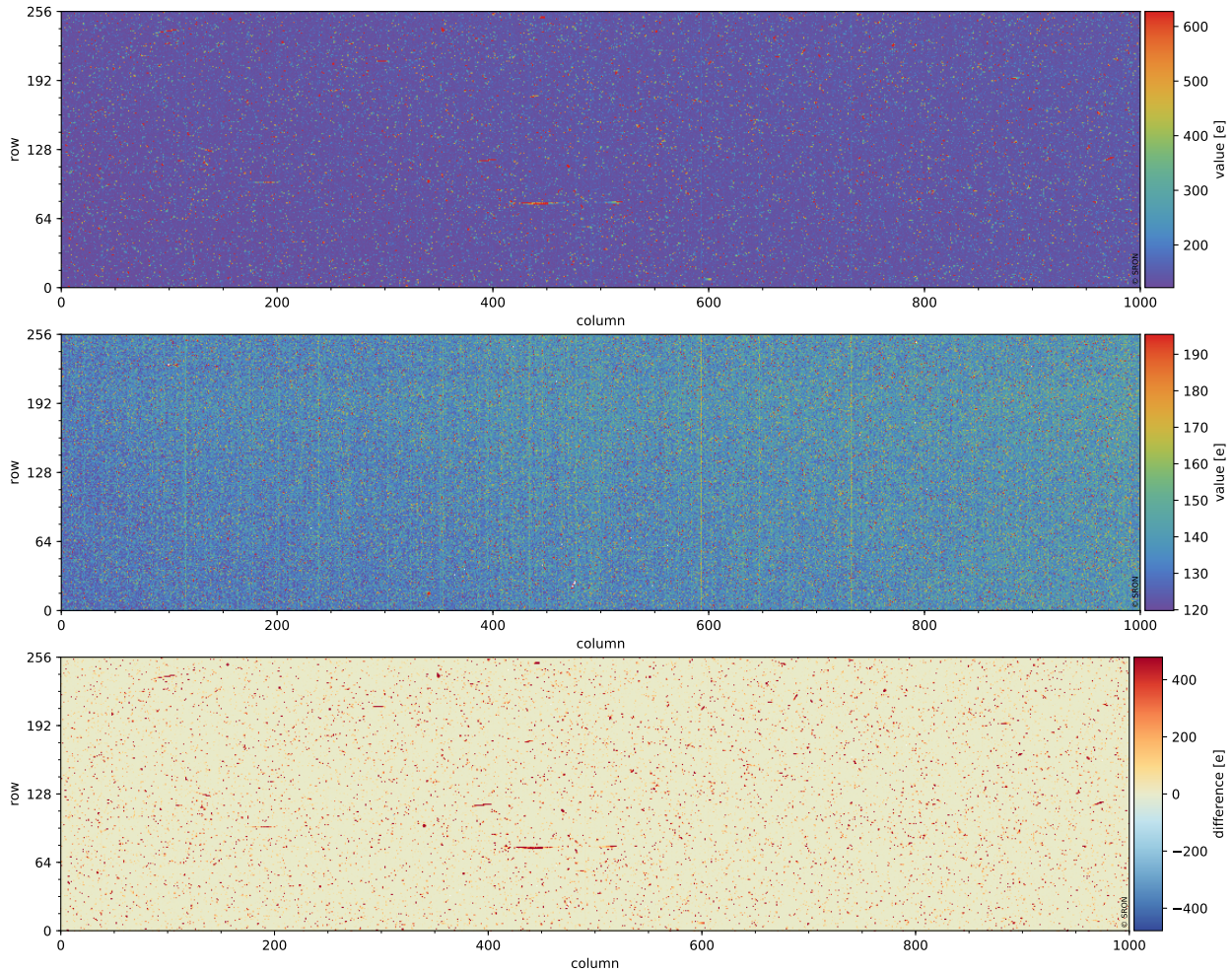
Figure 10. Noise of the SWIR detector measured during orbit 2707 to 2722 for an exposure time of 538.3 ms with the FMM closed, showing the noise calculated as a mean (top), median (middle) and the difference between the two (bottom).

Origin	bad quality	dead quality
on-ground	2283	258
orbit 1838	1686	215
orbit 2828	1730	217

Table 3. Number of detector pixels labelled as 'bad' (quality < 0.8) or 'dead' (quality < 0.1). Note that this does not cover the total of 250,000 detector pixels. The area used for retrieval, and adopted above, equals $\sim$210,000 pixels

on-board diffusers. Although monitoring of the transmission of the full optical train for radiance measurements is the main goal, it can only be approximated with the methods applied. Changes seen in the signal of the calibration sources and/or solar irradiance signals can originate from degradation of the sources, diffusers and/or any other optical elements in the optical path incl. the video chain. Both the calibration sources and diffuser are expected to degrade over the operational life-

time. After cross-calibration, any changes in the transmission should be carefully monitored and investigated. In this section we will compare the output of the on-board calibration sources and compare it to the results obtained on-ground.

3.4.1 DLED

The DLED is intended to monitor the stability of the detector. In-flight, monitoring of the detector signal caused by the DLED illumination is done by comparing the DLED response to a reference measurements taken late in the commissioning period. The reference measurement has in turn been calibrated to the on-ground reference.

Figure 13 shows the measurement of orbit 907 (Dec 2017) and 2707 (Apr 2018) as compared to the reference measurement, which was set to the measurement in orbit 2515. The DLED responses as seen in Figure 13 already show that the DLED has degraded between orbits 907 and 2707, relative to the reference orbit of 2515. However, typical degradation can be seen at a level of 0.1%. Features in the measurement
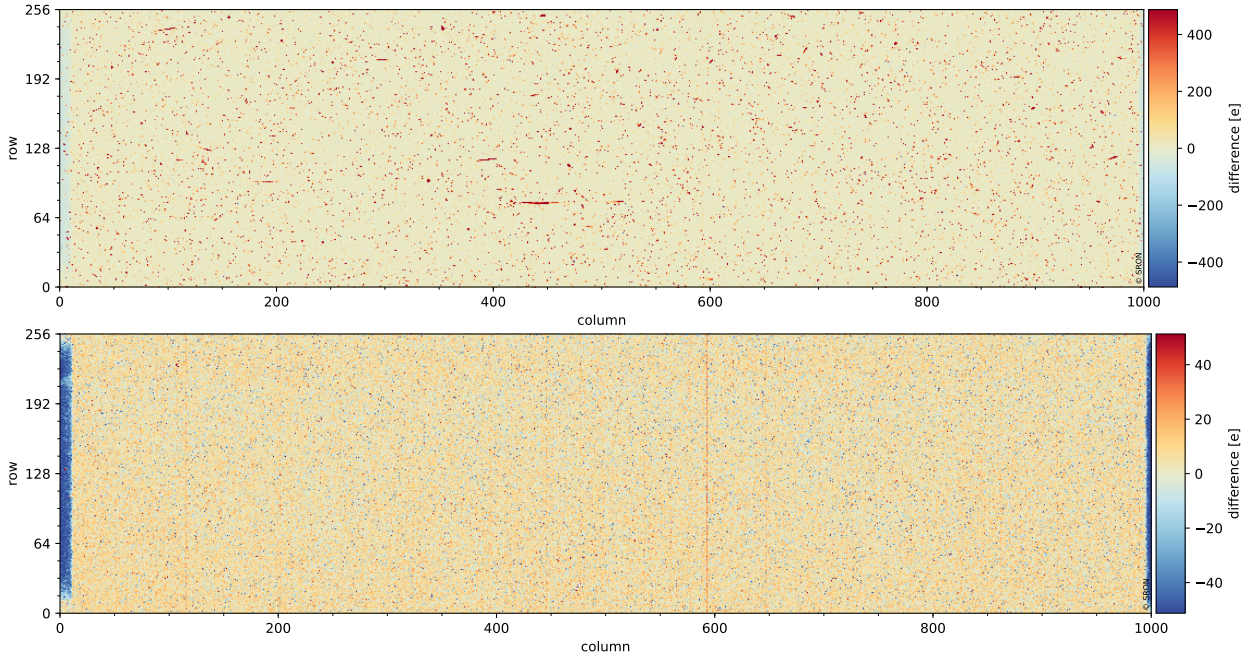
Figure 11. Comparison between the noise as measured in-flight during orbit 2707 to 2722 and on-ground. The top plot shows the difference between derivations using a root mean square while the bottom shows that using a bi-weight spread. Note that the similarity of the difference between on-ground and in-flight and the difference between the two methods as shown in the bottom part of Fig. 10.

.
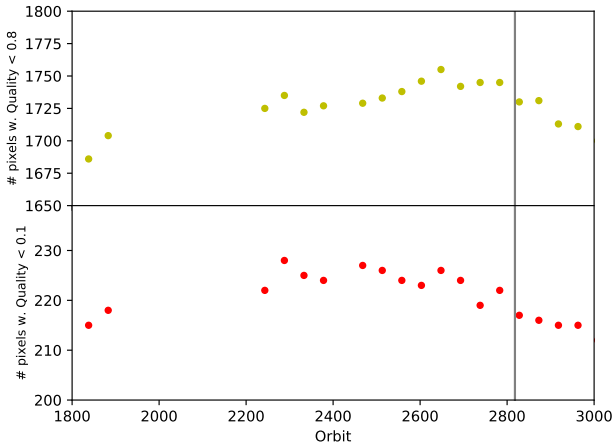
Figure 12. Number of dead (bottom red dots) and bad (top yellow dots) pixels. Pixel quality is expressed as a number between 0 and 1. The dotted line is a linear fit through the data.

of orbit 907 appeared after launch, and vanished, which is not well understood. It is hypothesized this is behaviour is either influenced by an etallon effect of a layer on the protective glass for the detector or a lens in the optical path of the DLED signal. The degradation is further discussed in section 4.5.

3.4.2 WLS

A Tungsten halogen lamp is mounted inside the calibration unit and acts as a white light source (WLS). Its output follows the complete light path within the module (see Fig. 1). The WLS settings have been optimized to yield sufficient signal in the UV and UVIS wavelengths. This results in a relatively strong output in the SWIR wavelength band. To avoid saturation, only measurements with a short exposure time (5 ms) are used for SWIR. The drawback is that due to small non-linearity effects, the uncertainties of the pixel and/or full array cannot reliably be determined. A reference for the WLS was derived at the end of phase E1 during orbit 2513. Given the much less stringent stability limits of the WLS system, no differences were found in the resulting SWIR signals. Changes and or small degradation seen in the SWIR signals of DLED fall within the measurement errors of an WLS measurement. This indicates that the optics of the SWIR module is stable over time.

3.5 Stray-light

The methodology to determine the stray-light calibration key data, including the on-ground measurements used, is described in detail in Tol et al. (2018). In-flight there is no capability to directly quantify the amount of stray-light within the SWIR module as a response to a point source illuminating any location of the SWIR detector. However, there is
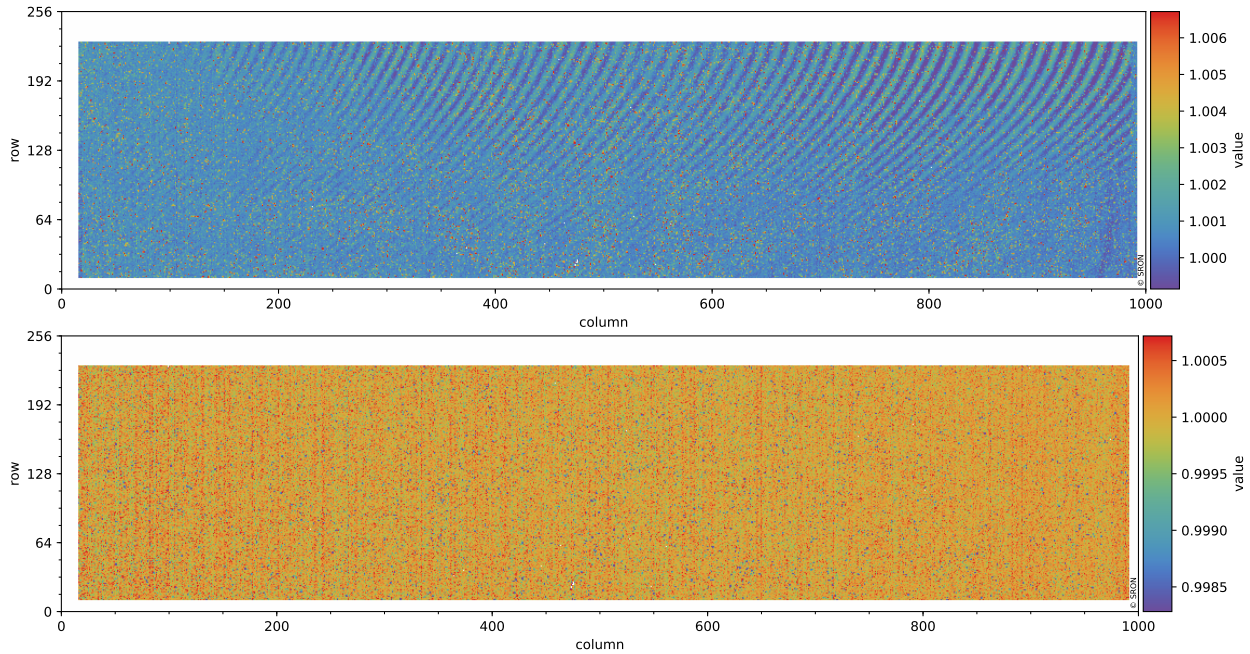
Figure 13. DLED response of orbits 907 (top) and 2707 (bottom), relative to the in-flight reference of orbit 2515. Note the change between orbits 2515 to 2707 is negligible.
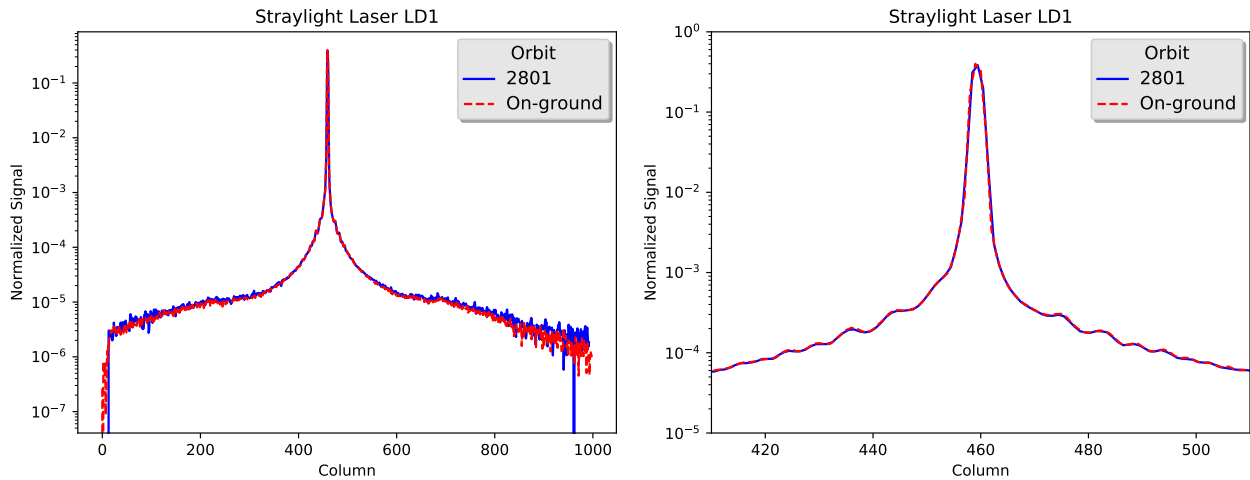

Figure 14. Comparison of in-flight measurements using SLS-1 during a single orbit with an identical measurement obtained during on-ground calibration. *Left plot* : full image. *Right plot*: zoom near the wavelength of SLS-1.

a possiblity to monitor the stability of the stray-light CKD over time by comparing the signal response of one of the on-board diode lasers that illuminates a spectral band with the equivalent on-ground measurement. Before launch, SLS-1 was selected for regular calibration measurements as its wavelength is located near the center of the SWIR band. The effectiveness of the stray-light CKD is checked by comparing the known signal response of SLS-1. Monitoring is done by merging a short (98 ms) and long (1998 ms) exposure. Frame merging is discussed in Tol et al. (2018), Section 3.

This method produces a frame with an unsaturated line centre while still retaining good signal-to-noise outer wings.

Figure 14 shows the spectral axis with medians taken over the swath for the on-ground and in-flight measurements for SLS-1. Stray-light is normalized over the total signal. Both the full dynamic range and a zoom around the laser wavelength are shown. This reveals no changes before and after launch in the distribution of the stray-light near the laser peak.
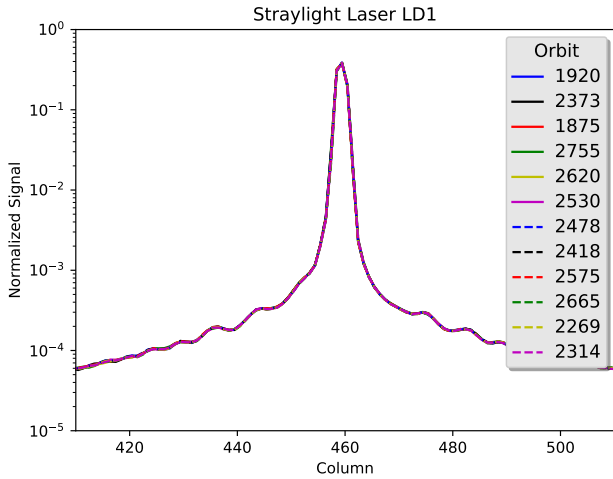
**Figure 15.** Results of all stray-light measurements with SLS-1 during the the E1 phase.

Orbit	Amount Stray-light [%]	Uncertainty $[10^{-2}\%]$
1875	2.90	2.3
1920	2.89	2.2
2269	2.91	2.2
2314	2.90	2.2
2373	2.93	2.3
2418	2.88	2.1
2478	2.89	2.3
2530	2.89	2.2
2575	2.91	2.2
2620	2.90	2.2
2665	2.89	2.2
2710	2.90	2.3
2755	2.93	2.3
2801	2.90	2.1

Table 4. Percentage of light detected on the SWIR detector outside of the central 15 pixels of a response to diode laser SLS-1 during the E1 phase.

Figure 15 shows all measurement taken with SLS1 during the the E1 phase, overplotted onto each other. This reveals that the amount and shape of stray-light has remained stable over the course of the first few months after launch. This is confirmed by the tracking of the amount of stray-light, seen in Table 4. The amount of stray-light is defined as all light seen outside the 15 spectral pixels centered on the laser peak. Note that this is not a direct quantification of the stray-light, but suffices as a monitoring quantity for the amount of stray-light.

3.6 ISRF

The Instrument Spectral Response Function (ISRF) of each pixel is required as input data for the gas-retrieval algorithms.
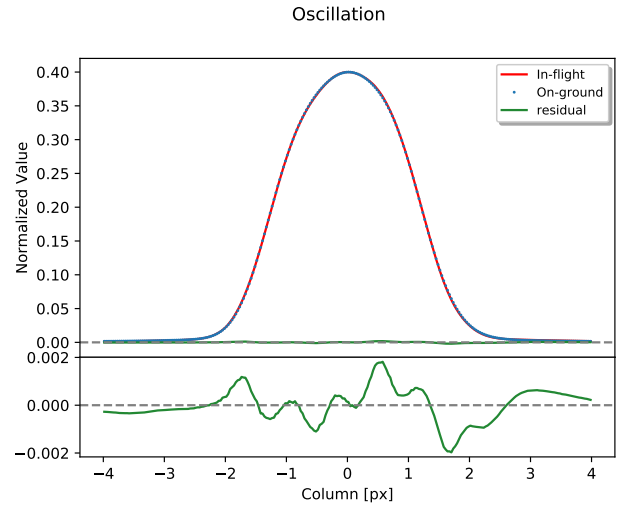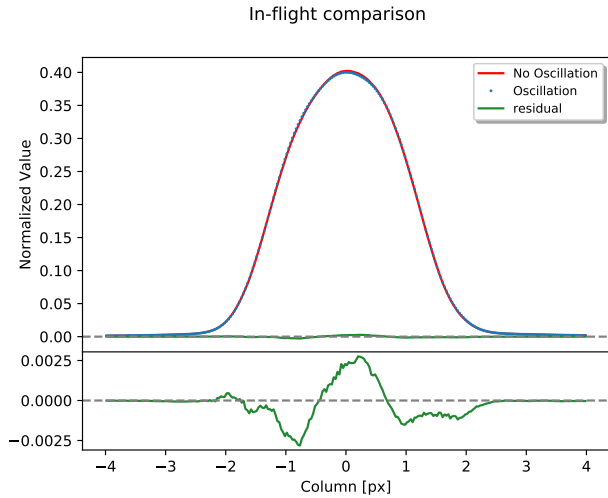

Figure 16. Comparison between the ISRF measurements taken during the on-ground calibration campaign and the E1 phase. *Top plot*: Normalized pixel response in-flight (red) and on-ground (blue). In green, the residuals are plotted. *Bottom plot*: Zoom of the residuals.
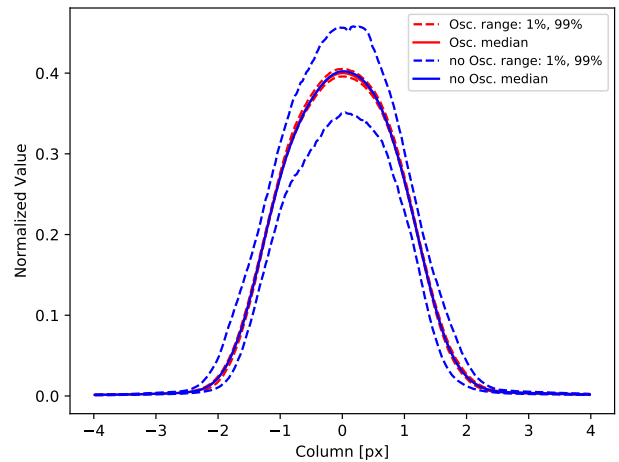
Figure 17. Comparison between the ISRF measurements taken with and without an oscillating diffuser. In red the measurements with an oscillating diffuser are plotted and in blue measurements without an oscillating diffuser.

The complete method to derive the ISRF CKD is described in van Hees et al. (2018). The CKD was derived using on-ground calibration measurements using an external tunable laser with the capability to illuminate limited parts of the swath. A method was proposed in van Hees et al. (2018) to monitor the ISRF using the on-board diode lasers. Each diode laser illuminates a different area on the SWIR detector (and thus probes different parts of the ISRF spectral parameter range). A local "monitoring" ISRF is derived from these measurements. As the diode laser illuminates the full spatial swath and the five lasers only sample very small ranges of

Figure 18. Comparison between the ISRF measurements taken with and without an oscillating diffuser. In-flight measurements during nominal operations are done without an oscillating diffuser. *Top plot*: Normalized pixel response in-flight (red) and on-ground (blue). In green, the residuals are plotted. *Bottom plot*: Zoom of the residuals.

the full spectral axis, the diode lasers cannot be used to derive ISRF CKD. Their use is to detect and monitor long-term changes in the ISRF, if any. During the E1 phase, the results from van Hees et al. (2018) were verified to determine any possible changes between on-ground calibration and phase E1 performance. At the same time, a checkout was performed of the diode laser settings for use during nominal operations (E2). In this paper results from diode laser SLS-1, which is the main reference during nominal operations, are presented, but all conclusions also apply to results obtained for the other four diode lasers.

Figure 16 shows the difference between measurements using diode laser SLS-1 carried out on-ground and in-flight. These were done using identical settings. In this figure, the normalized pixel response is compared by taking a median over the illuminated swath (220 rows) and normalizing over the total energy. The difference observed between in-flight and on-ground is less than 0.2% indicating no change of the instrument between on-ground calibration and phase E1. The measurements were done with an oscillating diffuser.

During nominal operations, diode laser measurements are carried out using a fixed diffuser instead of an oscillating diffuser. The oscillation is needed to randomize the speckles of the monochromatic laser. However, as the diffuser motion is a life limited item producing too much excess heat, it cannot be used during regular E2 monitoring. The resulting speckle pattern can be partially randomized by taking the median signal over all 220 rows illuminated. Figure 17 shows a comparison between in-flight measurements with identical settings except the (lack of) oscillation of the diffuser. In this plot the
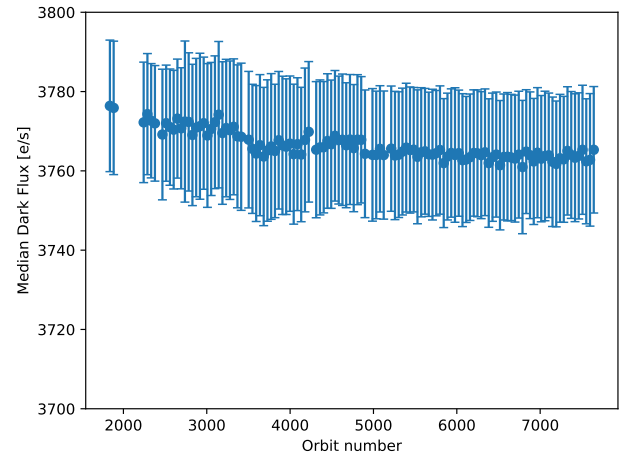
Figure 19. Median dark current as a function of time.
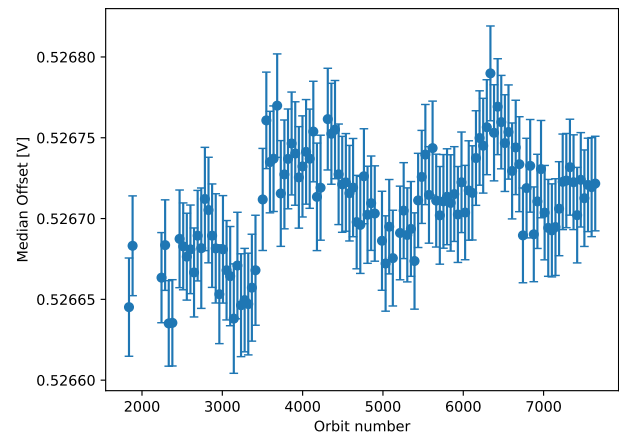
Figure 20. Median Offset as a function of time.

percentile range between 1 and 99 % is shown for all ISRF solutions in the spatial direction. It is clear that the range of solutions is much larger without an oscillating diffuser. However, the median ISRF solutions of both sets of measurements are very similar. Figure 18 shows this difference. From this figure it can be confirmed that the measured profile without an oscillating diffuser, although less accurate than the actual ISRF, is of sufficient quality to monitor the stability of the ISRF calibration in-flight. The figures in this section reaffirm that no changes larger than 0.2% are seen.

4   Monitoring Results during nominal operations

The performance of the SWIR module has been closely monitored since launch. At the end of phase E1, references were taken for the various monitoring paramters. In this section, the trends with respect to the reference are determined averaged over the full detector (i.e. either a mean or median of

the properties over the detector or the total amount of pixels flagged over the detector.). Interested readers are referred to the monitoring website of the SWIR module [9] for more information.

4.1 Background

Figure 19 and 20 show the detector median for the dark current and offset from February 20th 2018 to April 30th 2019. Both are extremely stable. Even on a per-pixel basis, variations are very small, on scales of a few electrons (or electrons per second in the case of dark current). Larger-scale variations seen during the monitoring have been exclusively caused by irregularities in the thermal controls, caused by orbit maneuvers (see http://www.sron.nl/tropomi-swir-monitoring/ for case studies). An example is the gap around orbit 3500, caused by an anomalous fault in the spacecraft, which caused the entire instrument to heat up. Data during such maneuvers are omitted in the data shown in Figures 19 and 20.

4.2 Noise

Figure 21 shows the median noise of of the SWIR detector as a function of time from February 20th 2018 for a year. There is some variation, but most is much smaller than the typical spread of the in-flight noise seen over the detector.

4.3 Detector Pixel Quality and Radiation impacts

Radiation impacts will gradually degrade the detector by causing pixels to become too noisy for retrieval or damage them to such a degree they stop functioning. Most of these impacts occur in the South Atlantic Anomaly.

Figure 22 shows the number of detector pixels flagged as bad or dead within the illuminated area from March 2018 to April 2019. Over this period, ~200 detector pixels had their quality value drop to below 0.8 and ~30 to below 0.1. A linear fit through all orbits gives a loss of 42 detector pixels per 1,000 orbits in the category bad and 6 detector pixels per 1,000 orbits in the category dead. When compared to the total amount of total pixels in the illuminated area (210,000 pixels), current estimates show that less than an additional 0.6% will be bad or dead at the end of the envisioned 7 years lifetime of TROPOMI. It is good to note that this assumes detector pixels are lost at the - currently observed - linear rate of 0.1% per year. However, if detector pixels are lost due to cumulative cosmic ray impacts, the rate likely will become non-linear at later stages during the lifetime. More in-depth analysis (i.e. using data from longer operational timescales) of the effects of cosmic ray impacts is warranted and planned for future work.

---

[9] http://www.sron.nl/tropomi-swir-monitoring/
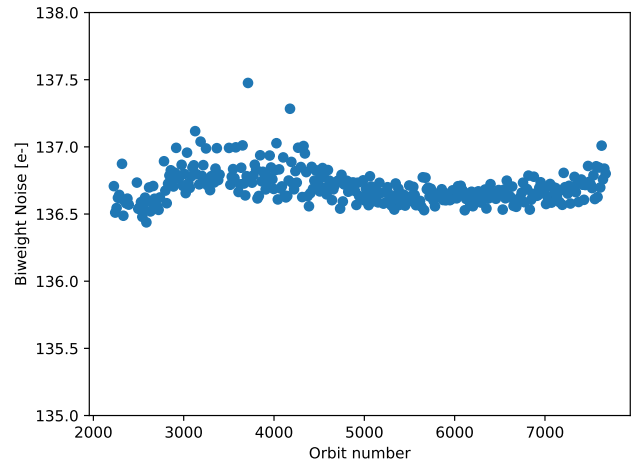
Figure 21. Median noise as a function of time. Large instabilities have been removed from this trend. Note that the median noise is insensitive for cosmic ray impacts.
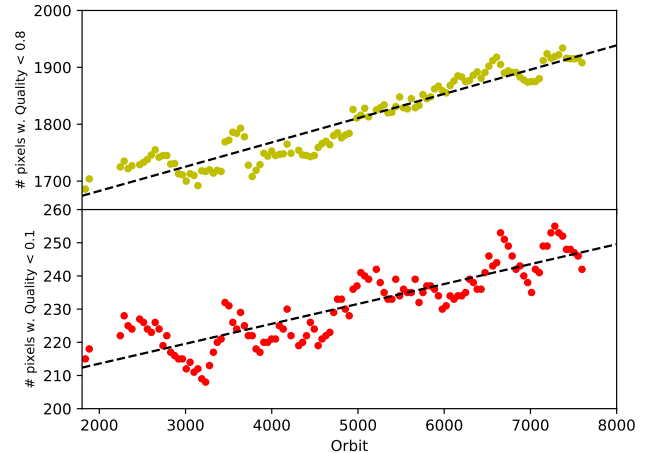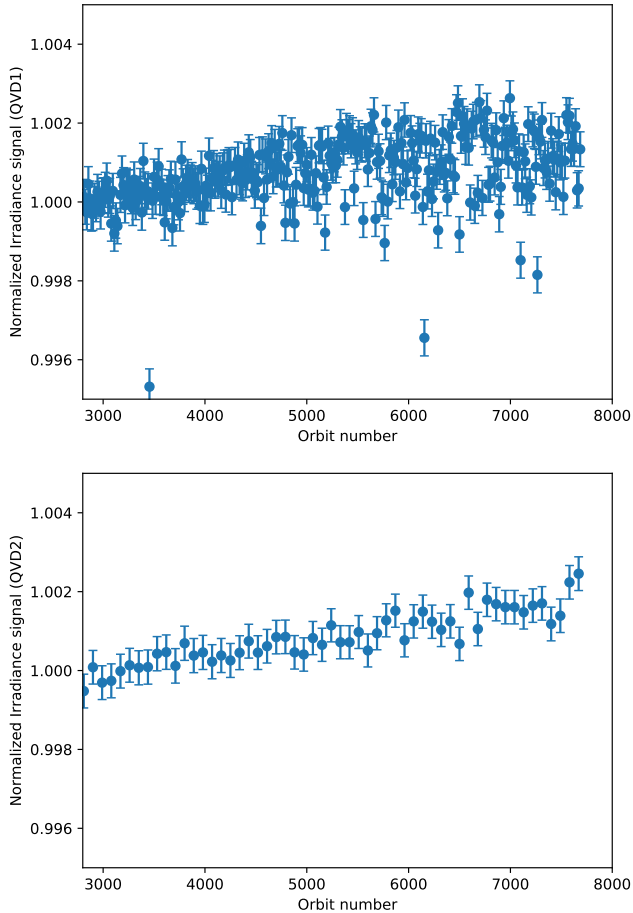

Figure 22. Number of bad (quality < 0.8, top image, yellow dots) and dead (quality <0.1, bottom image red dots) detector pixels since March 2018. A linear fit is shown with a black dashed line for each type. These have slopes of 42 and 6 detector pixels per 1,000 orbits for bad and dead detector pixels respectively.

4.4 Diffusers

Figure 23 shows the normalized response of the daily (which uses the main diffuser) or weekly (which uses the backup diffuser) solar irradiance measurements. Note that the diffusers are used for all four channels (UVN and SWIR) simultaneously. The diffusers do not appear to degrade at the SWIR wavelengths. NHowever, a long-term variance can be seen in both diffusers, with both diffusers apparently becoming more effective. This is hypothesized due to either an uncalibrated factor in the relative irradiance or a change in reflectivity of the diffuser. The latter can be attributed to the diffuser degradation seen at short wavelengths (Kleipool et al., pri-

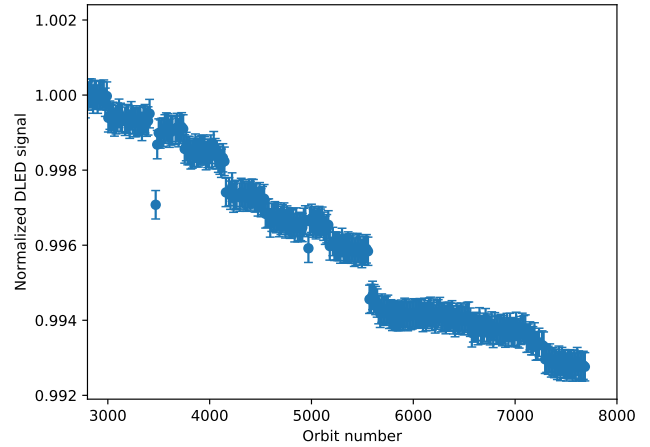**Figure 24.** Median Normalized DLED signal as a function of time.

Figure 23. Median normalized solar irradiance signal as a function of time. Top is the daily solar irradiance measurements, performed using the main diffuser QVD1. Bottom is the weekly solar irradiance measurement, performed using the backup diffuser QVD2.
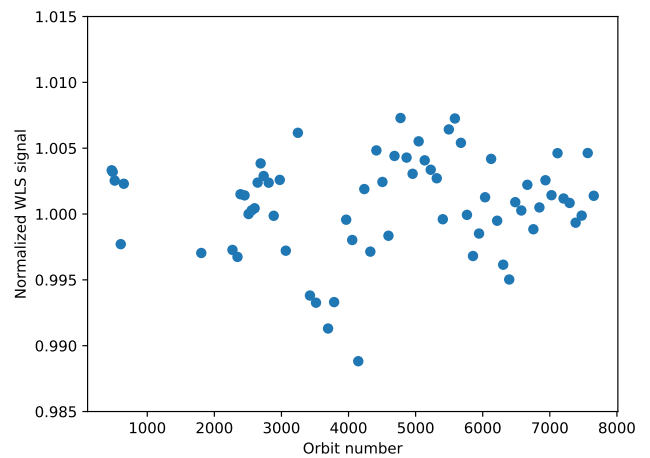

Figure 25. Median Normalized WLS signal as a function of time.

vate communication) in one, but not the other. Last but not least, actual solar variance due to the solar minimum in 2018 may explain small differences. Further study in the form of very long-term monitoring is required to understand the ob-
⁵ served slopes. As it is small, it has no observable effect on L2 products.

4.5   Stability of on-board calibration sources

Figures 24 and 25 show the normalized response of the DLED and WLS detector signals during nominal operations.
¹⁰ The DLED signal is degrading at a rate ∼0.8 % per year. The voltage fed to the DLED has been completely constant over the mission so far. Given the increase of the solar irradiance signals as seen in Figure 23 it is thus concluded that the DLED itself is degrading and not the detector respon-
¹⁵ sivity. However, more monitoring is required to confirm this hypothesis. Note that the outlier near orbit 3500 can be at-

tributed to a spacecraft anomaly during which the entire instrument heated up.

The WLS signal appears not to degrade. Note however that the accuracy of the WLS measurements is limited. The out- ²⁰ put of the WLS varies within ∼1% (+0.5%, -0.5%), compared to the reference measurement. In addition, the spread of the values around the median of each measurement also varies from measurement to measurement. However, degradation at levels seen for the DLED can be ruled out. It thus ²⁵ confirms a DLED degradation.

If we assume the DLED to degrade linearly, and given the envisioned lifetime of TROPOMI of seven years, the DLED is expected to lose 6% of its power output as compared to the start of nominal operations. ³⁰

4.6   ISRF

The stability of the ISRF is checked every month for each of the five diode lasers. Figure 26 shows the normalized

pixel response in orbit 5396 as compared to orbit 1667. Both measurements use identical settings. The difference is of the same order as seen in the comparison with the on-ground measurements, reported earlier in section 3.6. Monthly comparison reveal residuals of at most 0.2%. These residuals vary from measurements to measurements due to the speckles on the diffuser.
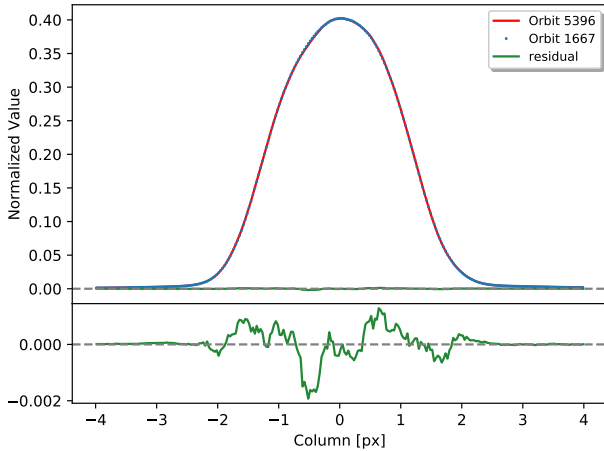

Figure 26. Comparison between the ISRF measurements taken during the E1 phase and in nominal operations, both without an oscillating diffuser. *Top plot*: Normalized pixel response in orbits 5396 (red) and 1667 (blue). In green, the differences are plotted. *Bottom plot* row: Zoom of the residuals.

4.7 Straylight

Stray-light monitoring is done once a month using diode laser SLS-1. Figure 27 reaffirms the conclusions and trend seen during the E1 phase. Stray-light is found to be very stable, with the amount of total stray-light seen as a response to a line source to be ~2.9%.

5 Conclusions

From the results as presented in section 3 of this paper, it can be concluded that the SWIR module did not change significantly between the on-ground calibration campaign and its first operations in space. This holds for all aspects: offset, dark current, detector noise, transmission, stray-light and ISRF. The results of the first year of nominal operations, as presented in section 4 of this paper, show that the SWIR module is very stable indeed on all aspects of the monitoring program. During the few orbit maneuvers that were needed to avoid collisions or to maintain formation flying with Suomi NPP, orientation of the satellite was lost resulting in nonnominal temperatures on board. Recovery to nominal temperatures was found to take hours for the SWIR detector and up to days for the SWIR spectrometer. During this time,
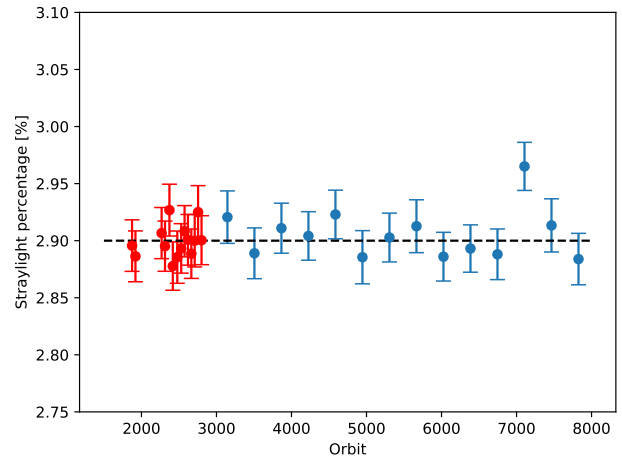
Figure 27. Results of all stray-light measurements with SLS-1 during the the E1 phase (red, see table 4) and nominal operations (blue) phases.

small deviations from the regular CKD may occur. Only if calibration measurements are scheduled can these be quantified. Data will be flagged in the data processer. The amount of pixels that have been lost so far is negligible (about 200 over a full year that are found to be bad, about 30 that are found to be dead), and given the current rate, less than 0.6% of the total amount of pixels will be lost over the envisioned operational time of 7 years, assuming a linear rate (which may not be true in case of accumulated radiation damage). With the condition of the TROPOMI-SWIR module as it is now, a very stable operational period is foreseen with little to no changes foreseen for the processer and on the calibration key data regarding SWIR products, yielding good quality Earth radiances to be used for accurate trace gas retrieval.

References

Beers, T. C., Flynn, K., and Gebhardt, K.: Measures of location and scale for velocities in clusters of galaxies - A robust approach, Astrophysical Journal, 100, 32–46, https://doi.org/10.1086/115487, 1990.

Hoogeveen, R., Jongma, R., Tol, P., Gloudemans, A., Aben, I., Vries, J., Visser, H., Boslooper, E., Dobber, M., and Levelt, P.: Breadboarding activities of the TROPOMI-SWIR module - art. no. 67441T, Carbon, 6744, https://doi.org/10.1117/12.737892, 2007.

Hoogeveen, R., Voors, R., Robbins, M. S., Tol, P. J. J., and I., I. T.: Characterization results of the TROPOMI Short Wave InfraRed detector, Proc.SPIE, 8889, 8889 – 8889 – 9, https://doi.org/10.1117/12.2028759, https://doi.org/10.1117/12.2028759, 2013.

Kleipool, Q., Ludewig, A., Babic, L., Bartstra, R., Braak, R., Dierssen, W., Dewitte, P.-J., Kenter, P., Landzaat, R., Leloux, J., Loots, E., Meijering, P., van der Plas, E., Rozemeijer, N., Schepers, D., Schiavini, D., Smeets, J., Vacanti, G., Vonk, F., and Veefkind, P.: Pre-launch calibration results of the TROPOMI payload on-board the Sentinel 5 Precursor satellite, Atmospheric Measurement Techniques Discussions, 2018, 1–67, https://doi.org/10.5194/amt-2018-25, https://www.atmos-meas-tech-discuss.net/amt-2018-25/, 2018.

Tol, P. J. J., van Kempen, T. A., van Hees, R. M., Krijger, M., Cadot, S., Snel, R., Persijn, S. T., Aben, I., and Hoogeveen, R. W. M.: Characterization and correction of stray light in TROPOMI-SWIR, Atmospheric Measurement Techniques, 11, 4493–4507, https://doi.org/10.5194/amt-11-4493-2018, https://www.atmos-meas-tech.net/11/4493/2018/, 2018.

van Hees, R. M., Tol, P. J. J., Cadot, S., Krijger, M., Persijn, S. T., van Kempen, T. A., Snel, R., Aben, I., and Hoogeveen: Determination of the TROPOMI-SWIR instrument spectral response function, Atmospheric Measurement Techniques, 11, 3917–3933, https://doi.org/10.5194/amt-11-3917-2018, https://www.atmos-meas-tech.net/11/3917/2018/, 2018.

Veefkind, J. P., Aben, I., McMullan, K., Förster, H., de Vries, J., Otter, G., Claas, J., Eskes, H. J., de Haan, J. F., Kleipool, Q., van Weele, M., Hasekamp, O., Hoogeveen, R., Landgraf, J., Snel, R., Tol, P., Ingmann, P., Voors, R., Kruizinga, B., Vink, R., Visser, H., and Levelt, P. F.: TROPOMI on the ESA Sentinel-5 Precursor: A GMES mission for global observations of the atmospheric composition for climate, air quality and ozone layer applications, rse, 120, 70–83, https://doi.org/10.1016/j.rse.2011.09.027, 2012.